Arch. Metall. Mater. **64** (2019), 4, 1577-1584

DOI: 10.24425/amm.2019.130129

ZHONGWEI MA*, QINGHUA LI*, LIN MA*#, ZHAOKUN HE**, ZHIMIN LIANG***

FATIGUE BEHAVIOR OF MIG-WELDED 7N01-T4 ALUMINUM ALLOY WITH DIFFERENT V-GROOVE ANGLES

7N01-T4 aluminum alloy was welded by metal inert gas welding and the influence of V-groove angle on joint fatigue properties was investigated. The results indicate that the volume of fusion zone (FZ) and the grains in FZ become small when the groove angle decreases to 50° from 70°. Most pores distribute at the FZ edge and fewer pores are formed in the small angle joint. The fatigue crack mainly initiates at the transition region between the weld passes due to the pore concentration. The small angle contributes to increasing joint fatigue properties, especially at the low stress level. The fatigue strength of 50° joint is 103.06 MPa which is 15.3% higher than that of 70°joint.

Keywords: 7N01-T4 aluminum alloy, MIG welding, V-groove angle, Fatigue, Fracture

1. Introduction

As a substitute of steel to reduce the weight of structure, aluminum alloy has an increasing application in the manufacturing fields of ship, aircraft and train due to its high specific strength [1,2]. 7N01 aluminum alloy is an Al-Zn-Mg alloy with excellent weldability and widely used in the big structural components. Welding is an indispensable method for the joining of such components. Although many novel welding methods, such as friction stir welding [3-7] and laser welding [8-11], have been rapidly developed in recent years, metal inert gas (MIG) welding still possesses a wide application in the joining of aluminum alloy especially the relatively thick plate owing to the mature technology, easy operation and high economy [12].

The structural component not only bears static stress but also experiences cyclic stress in many cases. Therefore, the fatigue failure is a potential threat to the structural reliability. Generally, the microstructure transform, stress concentration and plastic deformation are unavoidable for the welding joint, which makes the joint be the relatively weak position for the whole structural component and leads to the occurrence of fatigue fracture during the service life. The fatigue performance of MIG joint is always the research focus. Ni et al. [13] found that the fatigue fracture location of Al-5Zn-2Mg aluminum alloy MIG joint was related to the stress level. The fatigue fracture occurred at the heat affected zone (HAZ) when the stress level was lower than 50% of joint tensile strength, otherwise it occurred at the fusion zone (FZ). Guar et al. [14] found the surface-initiated failure was the main failure mode at low stress ratio ($\sigma_{min}/\sigma_{max} < 0.1$), while the defect-induced failure was predominant at higher stress ratio. Besides the stress state, the weld geometry is another essential factor influencing the joint fatigue performance. Ghosh et al. [15] found that the weld geometry was affected by the mean current and pulse frequency during the welding process, and the joint fatigue life was significantly increased when the ratio of the weld-top width to weld-bottom width was beyond ~0.56.

The weld geometry is also associated with the groove which is necessarily fabricated at the butt joint interface to deposit the weld metal and increase the depth of molten pool when it comes to the welding of medium or thick plate by MIG welding. The groove type is a significant control factor for the joint temperature history, FZ shape, HAZ size and welding residual stress [16]. As the most common groove type, V-groove attracts much attention. Chen et al. [17] studied the influences of groove angle on the heat transfer and fluid flow of MIG welding. The result showed that the groove with larger angle could facilitate the flow of molten pool but leaded to the appearance of coarser grains induced by overheat. Cho et al. [18] analyzed the molten pool behaviors in V-groove with and without root gap. They found that the root gap could facilitate the form of a fully penetrated weld bead in the flat and overhead positions. Giri et al. [19] concluded that the distortion and residual stress were increased with the increase of groove angle. These works indicate that the joint quality is strongly related to the groove geometry. However,

* SHENYANG AEROSPACE UNIVERSITY, SCHOOL OF AEROSPACE ENGINEERING, NO. 37 DAOYI SOUTH AVENUE, DAOYI DEVELOPMENT DISTRICT, SHENYANG 110136, CHINA.
** CRRC SIFANG CO., LTD, QINGDAO 266111, CHINA.
*** HEBEI UNIVERSITY OF SCIENCE AND TECHNOLOGY, SCHOOL OF MATERIAL SCIENCE AND TECHNOLOGY, SHIJIAZHUANG 050018, CHINA.
# Corresponding author: mlin128@163.com
Qinghua Li and Zhongwei Ma contributed equally to this work.

few literatures focus on the influence of groove angle on the joint fatigue performance. Therefore, the fatigue behavior of 7N01-T4 aluminum alloy MIG joint with different V-groove angles were investigated in this study, and the joint microstructure, tensile properties and hardness were also analyzed.

2. Experimental procedure

7N01-T4 aluminum alloy plates with the dimensions of 300 mm × 150 mm ×12 mm were used as the base material (BM). The filler wire was ER5356 with 1.6 mm diameter. The chemical compositions of BM and filler material are displayed in the Table 1. The shield gas was high-purify argon gas (99.999%) and the flow rate was 35 L/min. Before the welding, the BM was ground with sandpapers to remove the oxide film and then cleaned with acetone to remove surface inclusions. The V-type grooves with the angles of 50° and 70° were prepared on the BMs, respectively. The root gap was 2 mm (Fig. 1). The weld was completed in three passes and the process parameters were listed in the Table 2. After welding, the subsequent experiments were performed in a time interval of two weeks for natural ageing. The microstructure of the joint cross section was observed by an optical microscope (OM, Olympus-GX71). Before the observation, metallographic specimens were mechanically polished with emery papers, buff polished with 1 μm-diamond suspension and then etched by the Keller's reagent (1 ml HF+1.5 ml HCl+2.5 ml HNO_3+95 ml H_2O). The joint fracture was examined by the scanning electron microscope (SEM, SU3500). The tensile specimen size was determined according to ISO 4136:2001 and the schematic is displayed in the Fig. 2a. The tensile tests were performed at a speed of 3 mm/min. Vickers hardness was tested at the top, middle and bottom of the joint cross section, and the tested sites were located at the middle of the three weld passes, respectively. The load, dwell time and distance between the tested points were 200 g, 10s and 0.5 mm, respectively. The dimensions of fatigue specimen are displayed in Fig. 2b. The survival probability and confidence coefficient are 50% and 90%, respectively. Therefore, three fatigue specimens were tested at each stress level according to ISO 12107:2003. Prior to the fatigue tests, the specimens were ground and polished to remove the weld bulge and smooth surface. The uniaxial tension fatigue tests were performed at a stress ratio of 0.06. The stress was loaded in the form of sinusoidal wave and the frequency was 10 Hz. The fatigue test running until the occurrence of specimen fracture or specimen ran-out (10^7 cycles). The stress limit was considered as the maximum value of the applied sinusoidal stress at which the specimen survived 10^7 cycles.

TABLE 1

Chemical compositions of base material and filler material (wt.%)

Material	Zn	Mg	Cu	Cr	Mn	Ti	Si	Fe	Al
7N01-T4	4.6	1.2	0.2	0.2	0.15	—	0.35	0.4	Bal.
SAF-ER5356	0.1	5.1	0.1	0.07	0.01	0.1	0.18	0.25	Bal.

TABLE 2

Welding parameters

Groove angle (°)	Pass	Current (A)	Voltage (V)	Welding speed (mm/s)
70°	1	202	21	8.57
	2	180	20.2	4.48
	3	180	20.2	2.54
50°	1	212	22.4	8.33
	2	192	20.6	5.54
	3	192	20.6	4.69

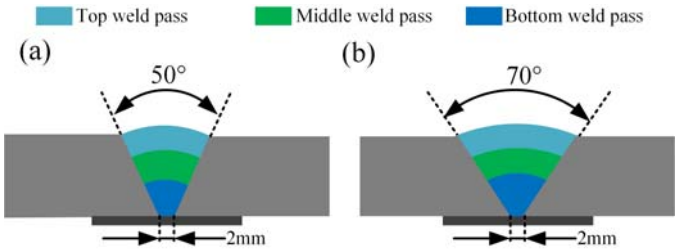

Fig. 1. Schematics of joints with V-groove angles of (a) 50° and (b) 70°

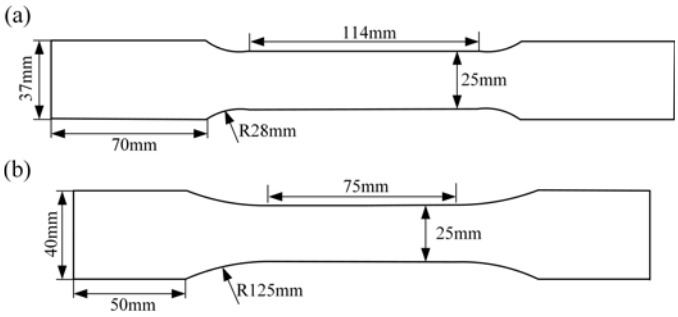

Fig. 2. Schematics of (a) tensile specimen and (b) fatigue specimen

3. Results and discussion

3.1. Microstructure

The cross sections of the MIG joints with different groove angles are displayed in the Fig. 3. No large pore, crack or impurity is observed. The joint can be divided into four zones: FZ, transition zone (TZ), HAZ and BM. The FZ presents a V-like shape, and the 50° joint has a smaller FZ compared with the 70° joint. The widths of FZ at top and bottom are 14.0 mm and 3.1 mm in the 50° joint, respectively. Those values increase to 19.4 mm and 5.3 mm in the 70° joint, respectively. The ratio of top width to the bottom width are 4.7 and 3.7 for the 50°and 70° joints, respectively. Ghosh et al. [15] found that increasing the ratio of top width to bottom width was beneficial to the improvement of joint fatigue properties.

The joint microstructures are displayed in the Fig. 4. It can be found that the BM is mainly comprised of the elongated grains (Fig. 4a). The HAZ experiences a heating process. Thus, the grains in this zone have an obvious growth, resulting in a larger

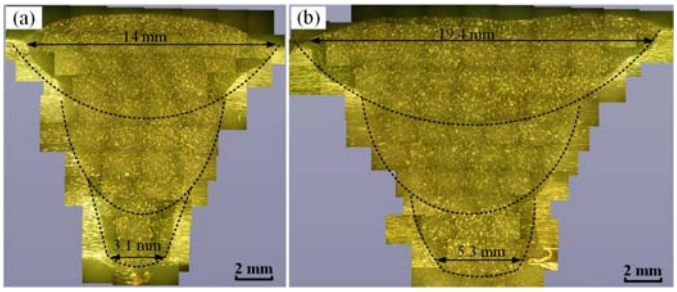

Fig. 3. Cross sections of (a) 50° and (b) 70° joints

grain size compared with that in the BM. The grain remelting occurs in the TZ, which results in a quite different microstructure compared with that in the adjacent zones. Zirconium is always added in the aluminum alloys to control sub-grain size and prevent recrystallization, which results in the formation of $ZrAl_3$ [20]. The formation of $ZrAl_3$ provides heterogeneous nucleation sites for the new grains during the solidification stage after welding [21]. Therefore, the layer consisting of fine-equiaxed grains is formed in the TZ (Fig. 4b and c). The fine-equiaxed grains increases the microstructural heterogeneity of joint due to the significant difference in the grain size. Due to the lower heat input, the TZ of 50° joint (Fig. 4b) is thinner than that of 70° joint (Fig. 4c). Directional columnar grains are formed near the edge of the FZ and these grains gradually transform into equiaxed grains from FZ edge to FZ center, which is induced by the inhomogeneous heat input and cooling rate in the FZ [22]. Figs. 4d-4f and Figs. 4g-4i display the FZ microstructures of 50 ° and 70° joints from the top weld pass to bottom weld pass, respectively. During the multiple-pass welding process, the material in the former weld pass experiences the additional heat input from the welding process of later weld pass. Therefore, the grain size presents an increasing trend from the top weld pass to bottom weld pass. Moreover, due to the lower heat input, the grains in the 50° joint are smaller compared with those in the 70° joint.

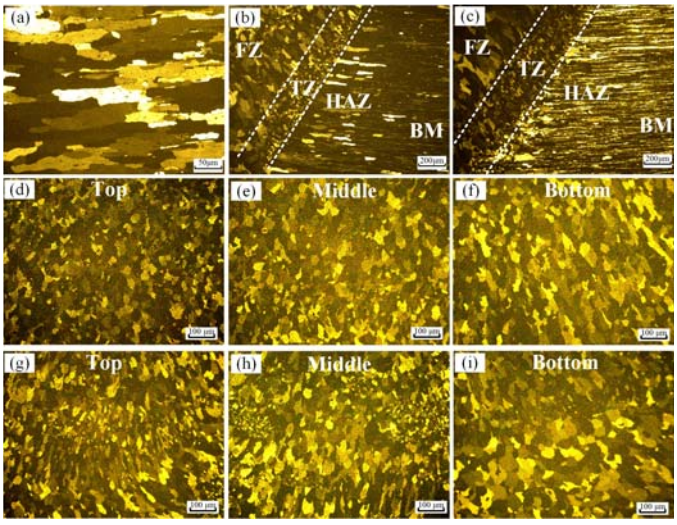

Fig. 4. Microstructures: (a) BM; TZs of (b) 50° and (c) 70° joints; (d) top , (e) middle and (f) bottom weld passes of 50° joint; (g) top, (h) middle and (i) bottom weld passes of 70° joint

3.2. Pore distribution

As shown in Fig. 5, nearly spherical pores are formed in the FZ because of the precipitation of supersaturated hydrogen [22]. The hydrogen solubility in the molten aluminum is higher than that in the solid-state aluminum. After welding, the solidification rate of the FZ is too high to provide enough time for the complete escape of supersaturated hydrogen, resulting in the formation of pores. The pores are difficult to be eliminated and their size and distribution have a significant influence on the joint mechanical properties. Since the region near the FZ edge has a higher cooling rate, more hydrogen is entrapped in this region. Therefore, the pores mainly distribute near the FZ edge. This phenomenon also corresponds to the found of Lefebvre et al. [23] and Huang et al. [24].

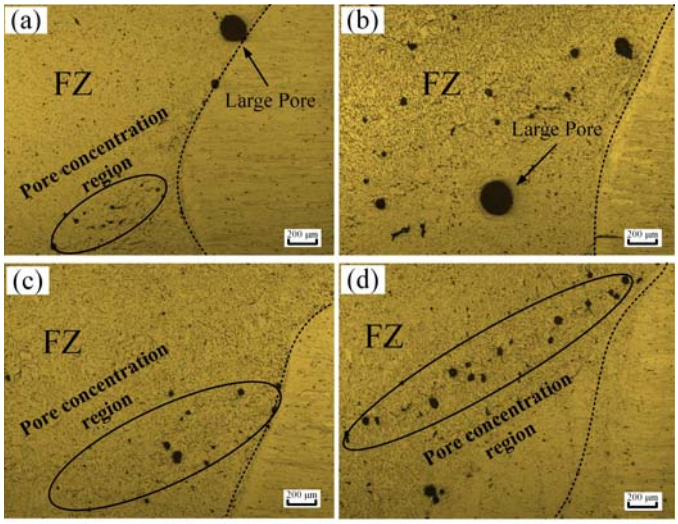

Fig. 5. Pore distribution at FZ edge: top weld passes of (a) 50° and (b) 70° joints; transition regions between middle and bottom weld passes of (c) 50° and (d) 70° joints

Figs. 5a and 5b display the pore distributions in the top weld pass of 50° and 70° joints, respectively. The pore diameter ranges from 10 μm to 300 μm. Pores with a larger size are rarely found, which may be attributed to that the large buoyancy force facilitates the escape of them from the FZ [24]. The larger pores tend to distribute at the top region and the smaller ones have a concentrated distribution at the lower region. Moreover, the lager pores are more nearly spherical in shape compared with the smaller pores. It may be because the geometry of small pore is more susceptible to the material flow and grain growth. It can be found that the pores are smaller and the density of the pores is lower in the 50° joint. Figs. 5c and 5d present the pore distribution in the transition zone between the middle and bottom weld passes. The material in the top region of the former weld pass is remolten due to the heating from the later weld pass. Hence, the unescaped large pores in the top region of the former weld pass are broken into the smaller pores by the intense material flow during the welding process of later weld pass. The small pores continue to float upward and eventually concentrate in the

transition zone between the two weld passes, resulting in the formation of pore concentrated region. The 50° joint possesses a smaller FZ, which decreases the region for the pore generation and results in a smaller amount of pores.

3.3. Hardness distribution

The hardness distributions at the top, middle and bottom weld passes of different joints are presented in the Fig. 6. According to Hall-Petch relationship, the hardness is decreased with the increase of grain size [25]. Fig. 4 has illustrated that the 50° joint possesses a smaller grain size compared with 70° joint, therefore the average hardness in the FZ of 50° joint is higher than that in the FZ of 70° joint. Due to the same mechanism, the hardness in the top weld pass (Fig. 6a) is higher than that in the middle (Fig. 6b) and bottom weld passes (Fig. 6c). The 50° joint possesses a smaller softening region compared with the 70° joint, which is attributed to the narrower FZ.

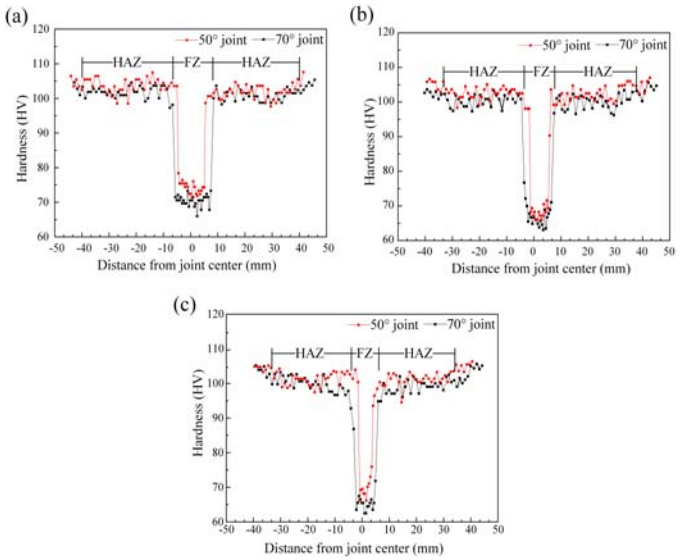

Fig. 6. Hardness distributions at (a) top, (b) middle and (c) bottom weld passes

The hardness firstly has a small decrease from BM to HAZ and then a severe decrease from HAZ to FZ. The width of the severe softening zone is decreased from the joint top to bottom, corresponding to the V-like shape of the FZ. 7N01-T4 aluminum alloy is an age-hardening alloy. Therefore, its hardness distribution is tightly associated with the change of precipitates besides the grain size [26]. During the welding process, the material in different zones of the joint experiences different heat cycles. It is reported that η ($MgZn_2$) is the main strengthen phase of 7N01-T4 alloy and its growth and dissolution temperatures are 150-300°C and 300-350°C, respectively [27]. The peak temperature can easily reach those ranges in the HAZ, which results in coarsening or dissolution of η phase and then the decrease of hardness. Generally, the HAZ can be further divided into two regions including dissolution region with a higher hardness and over-aging region with a lower hardness due to the difference in precipitate. However, such regions cannot be clearly distinguished in this study and the investigation of Yan et al. [28]. It may be because that the 7N01-T4 alloy possesses a relatively high natural aging effect after solid solution, and there is a time interval of two weeks between the hardness test and welding process. As for the FZ, the dissolution of strengthening precipitate occurs in the melting stage and non-precipitation occurs due to the quick solidification stage [29]. In addition, the filler metal ER5356 is a non-heat-treatable alloy and has a relatively low hardness [26]. These reasons lead to the loss of strengthening precipitate and then result in the severe softening of FZ. Moreover, Liu et al. [29] believed that the micro pores in FZ were also responsible to the hardness decrease. The lower heat input in the 50° joint is beneficial to reducing the loss of strengthening precipitate, which contributes to acquiring the higher joint hardness.

3.4. Tensile strength

The tensile properties of the different joints are displayed in the Fig. 7. The tensile strength and elongation of BM are 412 MPa and 15.3%, respectively. After welding, the joint tensile properties are lower than those of BM. The tensile strength and elongation of the 70° joint are 273.7 MPa and 6.8%, respectively. Those of 50° joint increased to 294.8 MPa and 7.6% which are 71.6% and 49.6% of BM, respectively. The larger elongation of 50° joint reveals a higher ductility which contributes to increasing the resistance of fatigue crack propagation. The tensile fracture is mainly located in the FZ, corresponding to the lowest-hardness region (Fig. 6). For the MIG welding, there are several factors limiting the increase of joint tensile properties. As shown in the Fig. 5, many micro pores with different sizes exist in the FZ, which reduces the area of load bearing and the joint ductility. The smaller FZ and the consequently less filler material in 50° joint are beneficial to reducing the pores and then improving tensile properties.

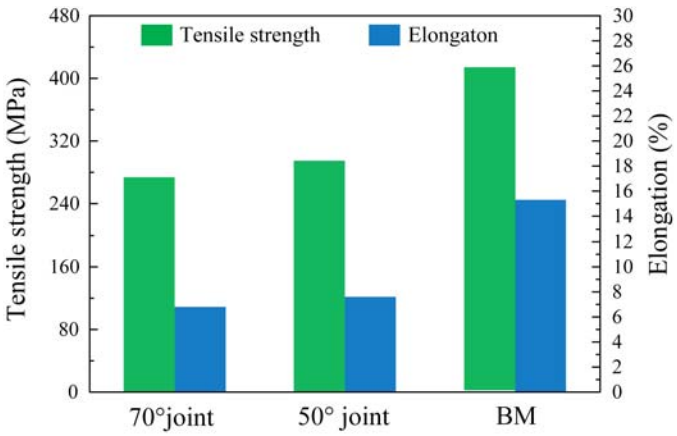

Fig. 7. Tensile properties of BM and different joints

4. Fatigue analysis

The results of the fatigue tests of 50° and 70° joints at different strength levels are listed in the Table 3. S is the maximum value of the uniaxial stress in the form of sinusoidal wave. N is the medium fatigue life calculated by the function of $N = \sqrt[n]{N_1 \cdot N_2 \ldots N_n}$. N_n is the joint fatigue life in the nth test. The S-N curves are expressed as the maximum stress S versus the corresponding medium life N to failure. This relationship can be obtained in the form of a power equation as flowing:

$$S^m \cdot N = C \tag{1}$$

Where C and m are the constants related to the material properties, specimen configuration, stress loading condition and so on. Generally, Eq. (1) is expressed in the form of Eq. (2), by which a linear relationship can be obtained:

$$S = A + B \lg N \tag{2}$$

Therefore, the data of S and N can be plotted in a semilogarithmic coordinate (Fig. 8). The data points with horizon arrow represent that the fatigue failure does not occur when the fatigue life reaches 10^7 cycles. The data fitting is performed according to Eq. (2) by the least squire method, and the fitting results of 50°and 70° joints are shown in Eq. (3) and Eq. (4), respectively.

$$S = 374.73 - 38.81 \lg N \tag{3}$$

$$S = 382.59 - 41.89 \lg N \tag{4}$$

The acquired fitting functions coincide well with the experiment results and the correlation coefficients of the fitting results of 50° and 70° joints are 0.901 and 0.954, respectively. Accordingly, the S-N curves are displayed in Fig. 8. It can be found that the gap between the curves of 50° and 70° joints is small at the low stress level, and the gap is increased with the decrease of S. The corresponding fatigue strength can be calculated by Eq. (3) and Eq. (4) with the aimed fatigue life of $N = 10^7$ cycles. As a result, the fatigue strength of 50° and 70° joints are 103.06 MPa and 89.36 MPa, respectively.

The joint fatigue properties are related to many factors including pore distribution, hardness distribution and microstructure of the joint. For the MIG welding joint, pore distribution is the predominant factor influencing the fatigue properties. The formation of pores not only reduces the load bearing area of the joint but also easily leads to the fatigue crack initiation due to the high stress concentration, which significantly deteriorates the

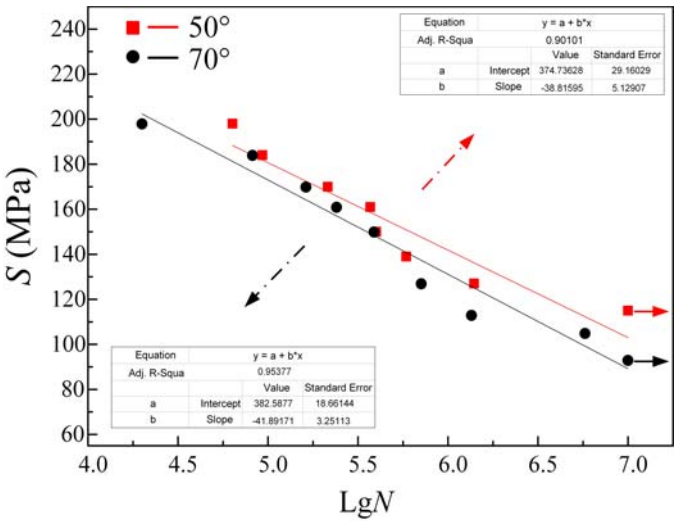

Fig. 8. S-N curves of different joints

joint fatigue strength. The pores in the 50° joint are fewer and smaller than those in the 70° joint (Fig. 5), which is the main reason leading to the improvement of fatigue strength. In regard to the microstructure, the decrease of grain size contributes to increasing the resistance to fatigue crack generation, which is beneficial to achieving longer crack initiation life [30]. Therefore, the finer grains in 50° joint have a positive influence on the joint fatigue properties. Besides the pores and grain size, hardness distribution is another essential factor influencing the joint fatigue properties. On one hand, the lowest-hardness region always corresponds with the weakest region for the joint, and the fatigue crack is prone to initiate at this region [31]. On another hand, Stanzl-Tschegg et al. [32] pointed out that high fatigue resistance could be achieved by homogenizing slip deformation so that the strain concentration was avoided. When the joint bears a tensile load, the strain mainly occurs at the local region with low hardness, which facilitates the intergranular slip and then fatigue crack initiation. A homogeneous distribution of hardness can reduce the strain concentration and then delay the fatigue crack initiation. Fig. 6 shows that the lowest hardness of the joint is located in the FZ, and the hardness in the 50° joint is higher than that in the 70° joint. The higher hardness in 50° joint improves the homogeneity of hardness distribution from HAZ to FZ, which alleviates the strain concentration and is beneficial to increasing the fatigue strength.

Fig. 9 displays the different fracture locations of fatigue specimens. Most of the specimens fracture at the FZ edge

TABLE 3

Results of fatigue tests

50° joint								
S/MPa	198	184	170	161	150	139	127	115
N	63555	93029	214768	369777	398951	585423	1395468	10^7<
70° joint								
S/MPa	198	184	170	161	150	127	113	105	93
N	19967	82044	162478	240403	388511	710128	1350032	5775133	10^7<

(Fig. 9a), and the others fracture near the FZ center (Fig. 9b). The fatigue fracture process includes three stages: fatigue crack initiation, fatigue crack propagation and final fast fracture [33]. The fracture morphologies with different crack initiation sites are displayed in the Fig. 10. In this study, the most common fatigue source leading to the crack initiation is the pore. Fig. 10a shows the internal fatigue crack source of the 70° joint at the stress level of 150 MPa with a relatively low fatigue life. Many pores concentrate in a banded region which is near the transition region of middle and bottom weld passes. It is worthy to note that this kind of crack source dominants a bigger percentage in 70 ° joint than that in 50° joint. The fatigue cracks initiate at many sites around the pore concentration region. After initiation, the crack confluence occurs at the propagation region, forming the bigger cracks which quickly extend upward and downward along the FZ edge. The appearance of the pore concentration region is the main reason for the fatigue specimen fracturing at FZ edge (Fig. 9a). Compared with the crack source in Fig. 10b, this kind of crack source provides more initiation sites, thereby resulting in a relatively low fatigue life. Fig. 10b shows the near-surface fatigue crack source of the 50° joint at the stress level of 150 MPa. A large pore with a diameter of ~400 μm is observed near the top surface of the joint. Compared with the pores inside the joint (Fig. 5), the pore near the joint surface has a larger size because of the growth tendency during floating upward process. The heat input in small angle joint is smaller than that in big angle joint, which shortens the time for the pore floating upward and further growth. The round shape and smooth inner surface of the large pore indicate that the large pore may result from the gas evolution during the welding process [24]. The pore near the joint surface is the main crack source leading to the specimens fracturing near the FZ center (Fig. 9b). Fig. 10c displays the fatigue crack initiation region with an inclusion as the crack source. The inclusion mainly derives from the filler material and the incomplete slag removal during the multiple-pass welding [26]. There exist many micro cracks around the inclusion due to the differences in the plasticity and coefficient of thermal expansion between the inclusion and the substrate of FZ. The micro cracks are prone to be the crack initiation sites under cycle tensile load.

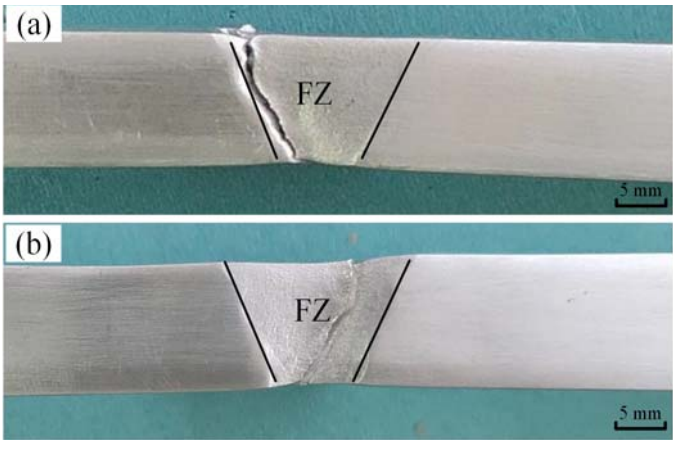

Fig. 9. Fracture locations: (a) at FZ edge and (b) near FZ center

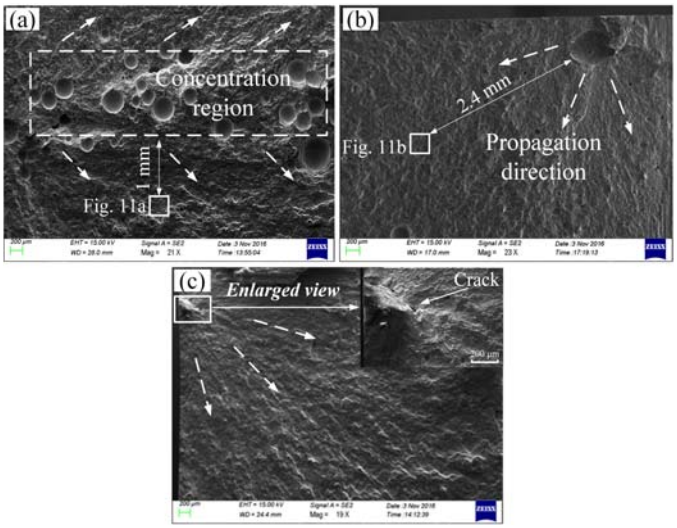

Fig. 10. Fatigue crack sources: (a) large pore near surface, (b) internal pore concentration and (c) inclusion

Compared with the big angle joint, the small angle joint needs fewer filler material. Therefore, it can be speculated that fewer inclusions exist in the 50°joint, which reduces the potential crack initiation site. After initiation, the fatigue crack propagates under the alternating stress and the radial pattern is formed in the propagation region (Fig. 10).

Fig. 11a shows the enlarged view of crack propagation region with a distance of ~1 mm from the crack source as marked in Fig. 10a. Many small terraces are formed in this region. Parallel fatigue striations spread over the terraces and are perpendicular to the crack propagation direction. Moreover, micro pores and second cracks can be observed between the striations. The micro pores in the propagation region easily lead to the stress concentration and then the formation of micro cracks, which reduces the crack propagation resistance. The enlarged view of the propagation region with a distance of ~2.4 mm from the crack source as marked in Fig. 10b is presented in Fig. 11b. Its surface is smooth compared with that in Fig. 11a and no micro pore or crack is observed. This difference is attributed to the different fracture locations between them. According to the Paris equation, the stress intensity factor at the crack tip is increased with the propagating of fatigue crack, which leads to a bigger propagation distance per cycle. Therefore, the distance between the striations in Fig. 11b is bigger than that in Fig. 11a.

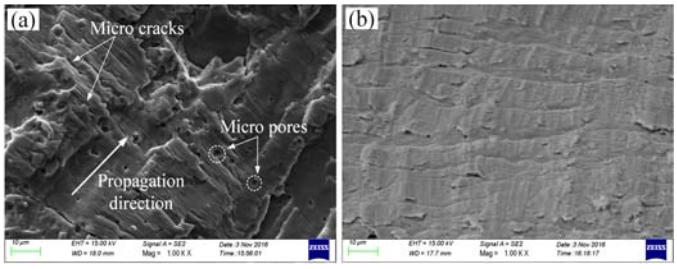

Fig. 11. (a) and (b) crack propagation regions marked in Fig. 10a and Fig. 10b

With the crack propagating, the bonding area of joint gradually becomes smaller. When it cannot bear the tensile load, the final fracture occurs. The final fracture regions of the 70° joint fracturing at FZ edge and the 50° joint fracturing near the FZ center are displayed in Figs. 12a and 12b, respectively. Numerous dimples are formed on both fracture surfaces, which indicates a ductile fracture. The fracture located near the FZ center (Fig. 12b) possesses larger dimples at the final fracture region compared with that located at the FZ edge (Fig. 12a). Under the tensile strength, micro voids are prone to nucleate at inclusions, second phase particles and grains boundaries, where plastic deformation discontinuity easily occurs [29,34]. The micro voids grow, coalesce and eventually form the dimples after fracture. Therefore, small second particles with the size of ~3 μm are observed in some dimples. The second particles may derive from the inclusions.

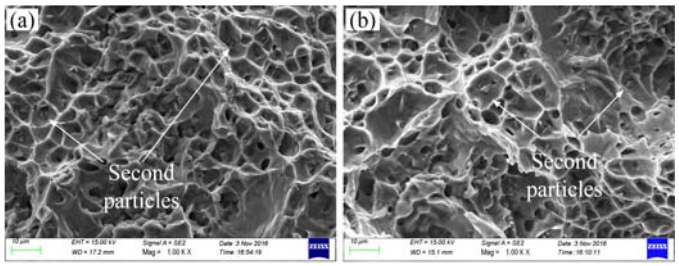

Fig. 12. Final fracture regions of (a) 70° joint fracturing at FZ edge and (b) 50° joint fracturing near FZ center

5. Conclusions

7N01-T4 alloy plates with 50° and 70°groove angles were welded by MIG welding, respectively. The uniaxial tension fatigue properties of the joints were mainly investigated and the following conclusions can be drawn.

(1) The FZ and the grains in FZ are smaller in the 50° joint compared with those in the 70° joint. Pores are mainly distributed in the FZ edge and have a concentrated distribution between the weld passes. Pores in the 50° joint are fewer and smaller.

(2) The softening degree is lower and softening area is smaller in the 50° joint. The tensile strength and elongation are 273.7 MPa and 6.8 % for the 70° joint, and these values increase to 294.8 MPa and 7.6% for the 50° joint, respectively.

(3) Fatigue specimens mainly fracture at the FZ edge due to the pore concentration and high microstructural heterogeneity. The pores near the joint surface account for the fatigue fracture located near the FZ center.

(4) The joint fatigue strength is increased by decreasing the groove angle from 70° to 50°. The fatigue strength of 50° joint is 103.06 MPa which is 15.3% higher than that of 70° joint.

REFERENCES

[1] S. Niu, S. Ji, J. Liu, X. Meng, J. Mater. Process. Technol. **267**, 141-151 (2019).

[2] Z. Ma, Y. Jin, S. Ji, X. Meng, L. Ma, Q. Li, J. Mater. Sci. Technol. **35** (1), 94-99 (2019).

[3] H.J. Liu, H. Fujii, M. Maeda, K. Nogi, J. Mater. Process. Technol. **142** (3), 692-696 (2003).

[4] Y. Huang, X. Meng, Y. Xie, L. Wan, Z. Lv, J. Cao, J. Feng, Compos. Part A Appl. Sci. Manuf. **105**, 235-257 (2018).

[5] V.C. Sinha, S. Kundu, S. Chatterjee, Arch. Metall. Mater. **62** (3), 1819-1825 (2017).

[6] W.F. Xu, Y.X. Luo, M.W. Fu, Mater. Charact. **138**, 48-55 (2018).

[7] Y. Huang, X. Meng, Y. Zhang, J. Cao, J. Feng, J. Mater. Process. Technol. **250**, 313-319 (2017).

[8] W. Piekarska, M. Kubiak, Z. Saternus, K. Rek, Arch. Metall. Mater. **58** (4), 1237-1242 (2013).

[9] M. Kallek, S. Ataoglu, Y. Yagci, H.N. Bozkurt, A.N. Gulluoglu, Arch. Metall. Mater. **57** (2), 525-537 (2012).

[10] M. Rózański, M. Morawiec, A. Grajcar, S. Stano, Arch. Metall. Mater. **61** (4), 1999-2008 (2016).

[11] S. Różowicz, S. Tofil, A. Zrak, Arch. Metall. Mater. **61** (2), 1157-1162 (2016).

[12] J.S. Shih, Y.F. Tzeng, J.B. Yang, Mater. Des. **32** (3), 1253-1261 (2011).

[13] W. Ni, S. Yang, J. Jia, J. Bai, Y. Lin., Rare Met. Mater. Eng. **45** (11), 2774-2778 (2016).

[14] V. Gaur, M. Enoki, T. Okada, S. Yomogida, Int. J. Fatigue. **107**, 119-129 (2018).

[15] P.K. Ghosh, S.R. Gupta, P.C. Gupta, R. Rathi, J. Mater. Sci. **26** (22), 6161-6170 (1991).

[16] Y. Ye, J. Cai, X. Jiang, D. Dai, D. Deng, Adv. Eng. Softw. **86**, 39-48 (2015).

[17] J. Chen, C. Schwenk, C.S. Wu, M. Rethmeier, Int. J. Heat Mass Transf. **55**, 102-111 (2012).

[18] D.W. Cho, S.J. Na, M.H. Cho, J.S. Lee, J. Mater. Process. Technol. **213** (9), 1640-1652 (2013).

[19] A. Giri, M.M. Mahapatra, K. Sharma, P.K. Singh, Int. J. Steel Struct. **17** (1), 65-75 (2017).

[20] C.E. Cross, Grong, M. Mousavi, Scr. Mater. **40** (10), 1139-1144 (1999).

[21] T. Koseki, H. Inoue, Y. Fukuda, A. Nogami, Sci. Technol. Adv. Mater. **4** (2), 183-195 (2003).

[22] Y. Liu, W. Wang, J. Xie, S. Sun, L. Wang, Y. Qian, Y. Meng, Y. Wei, Mater. Sci. Eng. A. **549**, 7-13 (2012).

[23] F. Lefebvre, I. Sinclair, Mater. Sci. Eng. A. **407** (1-2), 265-272 (2005).

[24] J.L. Huang, N. Warnken, J.C. Gebelin, M. Strangwood, R.C. Reed, Acta Mater. **60** (6-7), 3215-3225 (2012).

[25] S. Li, H. Dong, L. Shi, P. Li, F. Ye, Corros. Sci. **123**, 243-255 (2017).

[26] M. Nicolas, A. Deschamps, Acta Mater. **51** (20), 6077-6094 (2003).

[27] W. Sylwestrowicz, E. Hall, Proc. Phys. Soc. Sect. B. **64**(9), 495-502 (1951).

[28] Z. Yan, X. Liu, H. Fang, Int. J. Adv. Manuf. Technol. **91** (9-12), 3025-3031 (2017).
[29] S. Liu, J. Li, G. Mi, C. Wang, X. Hu, Int. J. Adv. Manuf. Technol. **87** (1-4), 1135-1144 (2016).
[30] Q. Dai, Z. Liang, G. Chen, L. Meng, Q. Shi, Mater. Sci. Eng. A. **580**, 184-190 (2013).
[31] C. He, Y. Liu, J. Dong, Q. Wang, D. Wagner, C. Bathias, Int. J. Fatigue. **82**, 379-386 (2016).
[32] S.E. Stanzl-Tschegg, O. Plasser, E.K. Tschegg, A.K. Vasudevan, Int. J. Fatigue. **21**, 18-22 (1999).
[33] Z. Ma, Y. Wang, S. Ji, L. Xiong, J. Manuf. Process. **36**, 238-247.
[34] J.F. Guo, H.C. Chen, C.N. Sun, G. Bi, Z. Sun, J. Wei, Mater. Des. **56**, 185-192 (2014).